

# JGR Space Physics

## RESEARCH ARTICLE

10.1029/2021JA029197

### Key Points:

- Defense Meteorological Satellite Program (DMSP) and Thermosphere Ionosphere Mesosphere Energetics and Dynamics (TIMED) satellites observed transpolar arcs (TPAs) in both hemispheres even during a prolonged radial interplanetary magnetic field (IMF) interval
- The TPAs can be categorized into two different types according to the precipitating particles and plasma drift velocity
- TPA formation is not limited to northward IMF conditions, and TPAs can occur on both closed and open field lines

### Supporting Information:

Supporting Information may be found in the online version of this article.

### Correspondence to:

J.-S. Park and Q. Q. Shi,  
[parkjspace@sdu.edu.cn](mailto:parkjspace@sdu.edu.cn);  
[sqq@sdu.edu.cn](mailto:sqq@sdu.edu.cn)



### Citation:

Park, J.-S., Shi, Q. Q., Nowada, M., Shue, J.-H., Kim, K.-H., Lee, D.-H., et al. (2021). Transpolar arcs during a prolonged radial interplanetary magnetic field interval. *Journal of Geophysical Research: Space Physics*, 126, e2021JA029197. <https://doi.org/10.1029/2021JA029197>

Received 30 JAN 2021

Accepted 23 MAY 2021

## Transpolar Arcs During a Prolonged Radial Interplanetary Magnetic Field Interval

Jong-Sun Park<sup>1</sup> , Quan Qi Shi<sup>1</sup> , Motoharu Nowada<sup>1</sup> , Jih-Hong Shue<sup>2</sup> ,  
Khan-Hyuk Kim<sup>3</sup> , Dong-Hun Lee<sup>3</sup> , Qiu-Gang Zong<sup>4</sup> , Alexander W. Degeling<sup>1</sup> ,  
An Min Tian<sup>1</sup> , Timo Pitkänen<sup>1,5,6</sup> , Yongliang Zhang<sup>7</sup> , I. Jonathan Rae<sup>8</sup> , and  
Marc R. Hairston<sup>9</sup> 

<sup>1</sup>Shandong Provincial Key Laboratory of Optical Astronomy and Solar-Terrestrial Environment, Institute of Space Sciences, Shandong University, Weihai, China, <sup>2</sup>Institute of Space Science, National Central University, Taoyuan, Taiwan, <sup>3</sup>School of Space Research, Kyung Hee University, Gyeonggi, South Korea, <sup>4</sup>Institute of Space Physics and Applied Technology, Peking University, Beijing, China, <sup>5</sup>Department of Physics, Umeå University, Umeå, Sweden, <sup>6</sup>Space Physics and Astronomy Research Unit, University of Oulu, Oulu, Finland, <sup>7</sup>The Johns Hopkins University Applied Physics Laboratory, Laurel, MD, USA, <sup>8</sup>Department of Space and Climate Physics, Mullard Space Science Laboratory, University College London, Dorking, UK, <sup>9</sup>William B. Hanson Center for Space Sciences, University of Texas at Dallas, Richardson, TX, USA

**Abstract** Transpolar arcs (TPAs) are believed to predominantly occur under northward interplanetary magnetic field (IMF) conditions with their hemispheric asymmetry controlled by the Sun-Earth (radial) component of the IMF. In this study, we present observations of TPAs that appear in both the northern and southern hemispheres even during a prolonged interval of radially oriented IMF. The Defense Meteorological Satellite Program (DMSP) F16 and the Thermosphere Ionosphere Mesosphere Energetics and Dynamics (TIMED) satellites observed TPAs on the dawnside polar cap in both hemispheres (one TPA structure in the southern hemisphere and two in the northern hemisphere) during an interval of nearly earthward-oriented IMF on October 29, 2005. The southern hemisphere TPA and one of the northern hemisphere TPAs are associated with electron and ion precipitation and mostly sunward plasma flow (with shears) relative to their surroundings. Meanwhile, the other TPA in the northern hemisphere is associated with an electron-only precipitation and antisunward flow relative to its surroundings. Our observations indicate the following: (a) the TPA formation is not limited to northward IMF conditions; (b) the TPAs can be located on both closed field lines rooted in the polar cap of both hemispheres and open field lines connected to the northward field lines draped over one hemisphere of the magnetopause. We believe that the TPAs presented here are the result of both indirect and direct processes of solar wind energy transfer to the high-latitude ionosphere.

## 1. Introduction

A particularly interesting phenomenon that occurs in the high-latitude ionosphere is the appearance of optical auroral arcs at magnetic latitudes (MLATs) poleward of the main auroral oval. The formation and evolution of these arcs in response to the solar wind and interplanetary magnetic field (IMF) conditions have been extensively studied over the past several decades, with the advent of satellite-based global observations of the arcs (Frank et al., 1982). A variety of names (i.e., transpolar arc, polar arc, oval-aligned arc, sun-aligned arc, theta aurora, and so on) has been used to describe such arcs in terms of their morphology (Kullen, 2012), although it is not clear whether they are generated by different mechanisms (see review by Zhu et al., 1997). In this study, we refer to the auroral arcs formed within the polar cap as transpolar arcs (TPAs) to avoid any confusion in terminology among them.

Previous studies reported the characteristics of TPA formation in relation to the IMF orientation. For the north-south component of the IMF (IMF  $B_z$ ), TPAs predominantly occur under northward IMF conditions (Ismail & Meng, 1982; Ismail et al., 1977; Kullen et al., 2002; Valladares et al., 1994) during intervals of low geomagnetic activity (Berkey & Kamide, 1976; Ismail et al., 1977). Although the TPAs occurring under northward IMF conditions could retain their form under southward IMF intervals (Valladares et al., 1994), these auroral structures usually start to dissipate after the southward turning of the IMF with a time delay

up to  $\sim 1$  h (Rodríguez et al., 1997). These observational results imply that the particles producing TPAs originate in the tailward side of the cusps, rather than in the sunward side of them.

The characteristics of TPAs in response to the dawn-dusk component of the IMF (IMF  $B_y$ ) are more complicated than for IMF  $B_z$ . It is not clear whether a sign change of IMF  $B_y$  triggers the TPAs (e.g., Kullen, 2000; Tanaka et al., 2004) or not (e.g., Fear & Milan, 2012; Milan et al., 2005). However, it has been pointed out that the magnetic local time (MLT) at which stationary TPAs form depends on the sign of IMF  $B_y$ , in such a way that under dawnward (duskward) IMF conditions, TPAs are located on the dawnside (duskside) of the polar cap in the northern hemisphere (Gussenhoven, 1982; Kullen et al., 2002) and on the duskside (dawnside) in the southern hemisphere (Gusev & Troshichev, 1986; Østgaard et al., 2005). Fear and Milan (2012) found that the most favorable location for TPA formation indeed depends on IMF  $B_y$  with the highest correlation for  $\sim 3$ –4 h delay time prior to the TPA onset. Moreover, it has been revealed that the direction of motion of TPAs can also be determined from the sign of IMF  $B_y$  in such a way that the TPA moves downward (duskward) in the northern hemisphere and duskward (dawnward) in the southern hemisphere for dawnward (duskward) IMF conditions (Carter et al., 2017; Fear & Milan, 2012; Kullen, 2000; Xing et al., 2018). Hosokawa et al. (2011) divided TPAs into two groups according to their motion in response to the IMF  $B_y$  orientation (IMF  $B_y$ -dependent TPAs and IMF  $B_y$ -independent TPAs) and suggested that the IMF  $B_y$ -dependent TPAs could be on open field lines (connected directly to the IMF) or on closed field lines (rooted on the Earth) adjacent to the open-closed magnetic field boundary, whereas the IMF  $B_y$ -independent TPAs could be on closed field lines. These results imply that the origin of the particles producing the two TPA types could be different.

Compared to the other IMF components, very little attention has been paid to the contribution of the Sun-Earth component of the IMF (IMF  $B_x$ ) to the TPA formation. It has been suggested that TPAs occur more frequently in the northern (southern) hemisphere under earthward (sunward) IMF  $B_x$  conditions due to the nonconjugate access of solar wind particles to the polar cap (Ismail & Meng, 1982) and the difference in intensity of the flow shear (and electric field) between the north and south polar caps (Østgaard et al., 2003, 2005). However, previous studies focused on nonconjugate TPAs in relation to the IMF  $B_x$  orientation coupled to northward IMF, and their results led to conclusions in terms of the controlling drivers that suppress TPAs. Therefore, it is still difficult to distinguish the origin of the particles that produce the TPA between solar wind electrons precipitating along open field lines (e.g., Carlson & Cowley, 2005; Hardy et al., 1982) and plasma sheet (and its boundary layer) electrons precipitating along closed field lines (e.g., Fear et al., 2014; Milan et al., 2005), with respect to the IMF  $B_x$  orientation.

Although the IMF usually follows the Parker spiral configuration (Parker, 1958), spacecraft observations in near-Earth space have shown that the IMF is occasionally nearly aligned with the Sun-Earth line on a timescale of more than several hours, defined as a prolonged radial IMF interval (Neugebauer & Goldstein, 1997; Neugebauer et al., 1997). During radial IMF intervals, the field lines draped southward and northward about the magnetopause lead to magnetic reconnections sunward of the cusp in one hemisphere and tailward of it in the other hemisphere (Pi et al., 2017; Tang et al., 2013), in addition to magnetotail reconnection that generates closed field lines (Tang et al., 2013). Wang et al. (2014) examined the characteristics of the field-aligned currents (FACs), ionospheric convection, and auroral activity in response to radial IMF and showed that north-south hemispheric asymmetry in solar wind energy input to the polar cusp ionosphere exists under these conditions. They proposed that such asymmetry is closely related to the different topology of the terrestrial magnetic field lines connected to the radial IMF between the hemispheres.

In this study, we first present interhemispheric observations of TPAs during a prolonged radial IMF interval. The characteristics of precipitating particles and plasma flow in the TPA regions are examined in order to infer the field line configuration connected to these regions. This study is organized into five sections as follows. The data set used in this study is introduced in Section 2. Our observations (interplanetary and geomagnetic conditions, auroral emissions, precipitating particles, plasma flow, and magnetic perturbations) are presented in Section 3. In Section 4, we discuss the terrestrial magnetic field topology associated with the TPAs under radial IMF conditions based on our observational results. Section 5 provides conclusions.

## 2. Data Set

In this study, we show auroral images deduced from remote-sensing observations of far ultraviolet (FUV) emissions by the Special Sensor Ultraviolet Spectrographic Imager (SSUSI) aboard the Defense Meteorological Satellite Program (DMSP) F16 satellite (Paxton et al., 1992) and the Global Ultraviolet Imager (GUVI) aboard the Thermosphere Ionosphere Mesosphere Energetics and Dynamics (TIMED) satellite (Christensen et al., 1994; Paxton et al., 1999) in order to present the TPAs occurring in both hemispheres during the prolonged radial IMF interval on October 29, 2005.

The IMF and solar wind data provided by the OMNI database (King & Papitashvili, 2006) are time-shifted from a solar wind monitor to the nominal bow shock nose (Farris & Russell, 1994). We use 5-min-averaged OMNI IMF data to identify a prolonged interval of radial IMF that is exerted on the bow shock. The OMNI solar wind data (solar wind speed and proton number density data at a 5-min resolution) are also used to examine the solar wind properties in the event studied. We note that short timescale (less than tens of seconds) disturbances in IMF/solar wind parameters that make it difficult to identify the long-duration radial IMF event are not considered using the 5-min resolution data.

DMSP F16/SSUSI as well as TIMED/GUVI provides cross-track scanned images of FUV emissions in five different wavelengths (Christensen et al., 1994; Paxton et al., 1992): 121.6 nm, 130.4 nm, 135.6 nm, and two Lyman-Birge-Hopfield (LBH) bands ( $\sim 140$ – $150$  nm short band and  $\sim 165$ – $180$  nm long band). Of the five different wavelengths, FUV emissions in the LBH short (LBHS) and long (LBHL) bands are due to impact of primary precipitating particles and secondary electrons (the electrons created by ionization of neutral particles) on the molecular nitrogen ( $N_2$ ) in the atmosphere. In this study, we use FUV emissions measured in the LBHS band to identify the TPAs.

In addition to auroral emissions, the characteristics of electrons and ions (with energy ranges from  $\sim 30$  eV to  $\sim 30$  keV) precipitating into the TPA regions are examined using their differential energy fluxes recorded every second by the Special Sensor for Precipitating Particles, version 4 (SSJ/4) sensor (Hardy et al., 1984) on board the DMSP F13 satellite and version 5 (SSJ/5) sensor (Hardy et al., 1993, 2008) on board the DMSP F16 satellite. The ionospheric plasma flows in the TPA regions are also examined using the horizontal cross-track ion velocity data acquired using the Special Sensor for Ions, Electrons, and Scintillation (SSIES) instruments on board the DMSP F13 (SSIES-2) and F16 (SSIES-3) satellites (Rich, 1994). For each version of the SSIES instruments, the horizontal cross-track ion velocity data (4-s cadence for SSIES-2 and 1-s cadence for SSIES-3) are quality flagged (“good”, “caution”, “poor”, and “undetermined”) based on the total ion density and the fractional composition of oxygen ions (Hairston, 2018). In this study, we mainly use the horizontal cross-track ion velocity data flagged as “good” and (use with) “caution”. The data flagged as “undetermined” are used depending on the circumstances, that is, if they are consistent in trend with determined data obtained in the surrounding region (Hairston, 2018). We avoid using the data flagged as “poor”.

In order to infer the TPA-associated FAC system, we examine magnetic perturbations using the data for the residual magnetic field vector, defined as the difference between the magnetic field vector (1-s cadence) measured by the Special Sensor Magnetometer (SSM) instrument on board the DMSP satellites (Rich, 1984) and the Earth's main magnetic field vector given by the International Geomagnetic Reference Field model (that is,  $\delta B_i = B_i - B_{i,IGRF}$ , where  $i = x, y$ , and  $z$  in spacecraft-centered coordinates). In the spacecraft-centered coordinate system applied to the DMSP/SSM data,  $\hat{x}$  points to spacecraft nadir (that is, positive downward along the local vertical direction),  $\hat{y}$  points to the direction of the spacecraft velocity vector, and  $\hat{z}$  (cross-track component) completes the right-hand orthogonal system. A fraction of the actual FAC density ( $j_x$  in spacecraft-centered coordinates) is then estimated from the single-satellite magnetic field measurements (Lühr et al., 1996) as

$$j_x = \frac{1}{\mu_0 v} \frac{\Delta \delta B_z}{\Delta t} \quad (1)$$

where  $\Delta \delta B_z$  is the spatial gradient of the residual cross-track magnetic field component (defined as  $\Delta \delta B_z(t) = \delta B_z(t + \Delta t) - \delta B_z(t)$ ),  $\Delta t$  is the sampling rate (1-s cadence for DMSP/SSM data),  $v$  is the spacecraft speed ( $\sim 7.5$  km/s for DMSP satellites), and  $\mu_0$  is the vacuum permeability. Equation 1 implies that the upward (downward) FAC sheet is characterized by a region of negative (positive) gradient in  $\delta B_z$  along the

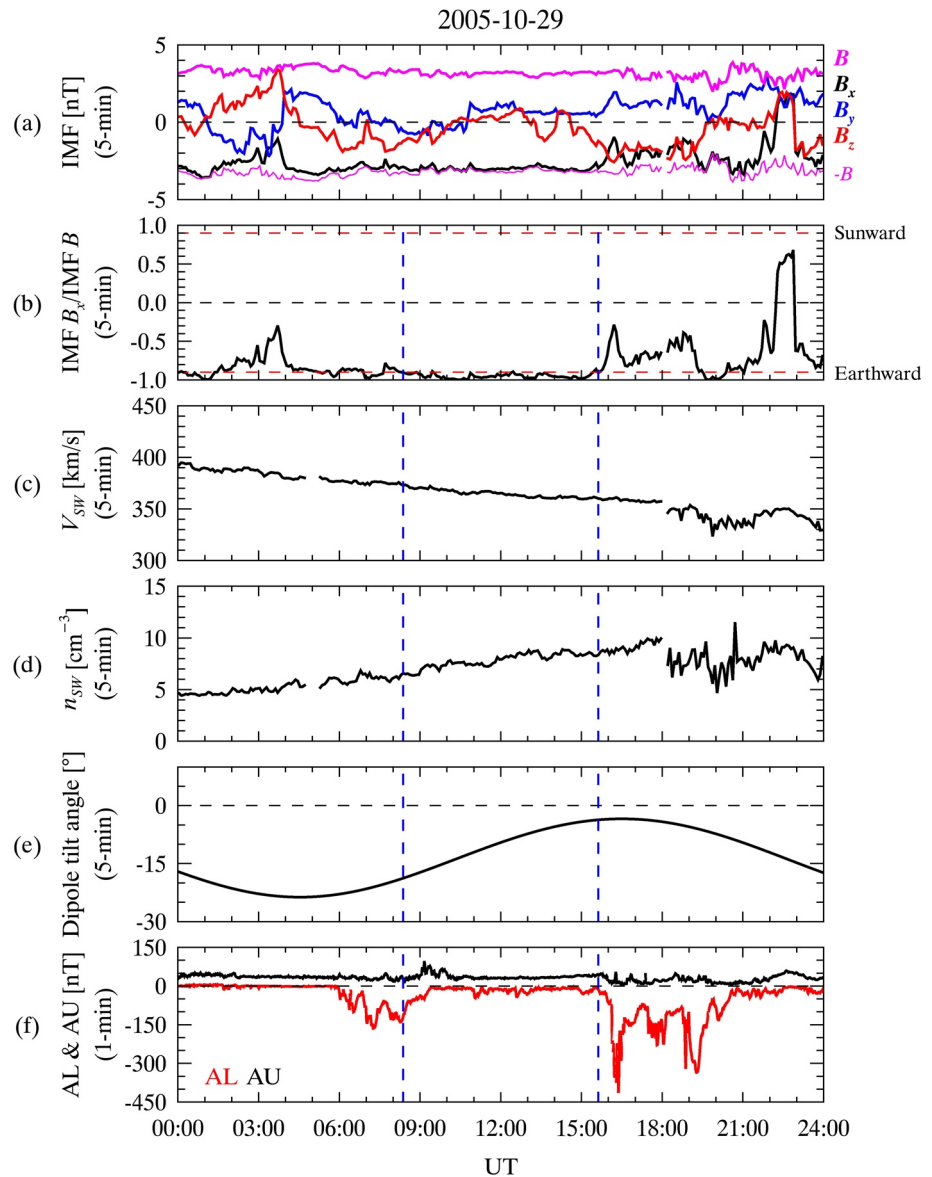


**Figure 1.** One-day overview of (a) the vector components of interplanetary magnetic field (IMF) (black, blue, and red lines for IMF  $B_x$ , IMF  $B_y$ , and IMF  $B_z$ , respectively, in geocentric solar magnetospheric [GSM] coordinates) and the magnitude of it (thick magenta line for IMF  $B$  and thin magenta line for  $-IMF B$ ), (b) IMF  $B_x$  / IMF  $B$ , (c) solar wind speed, (d) number density of protons, (e) dipole tilt angle, and (f) AL (red) and AU (black) indices on October 29, 2005. The time resolutions for the parameters are denoted in each panel. Two vertical dashed lines in Figures 1b–1f denote the earthward IMF interval.

DMSP satellite track. Because we are interested in the FAC density profile in the high-latitude ionosphere (inside the auroral ovals), the influence of the angle between the background magnetic field and the  $x$ -axis (in spacecraft-centered coordinates) on the FAC density is neglected. Moreover, we assume that the satellite track is perpendicular to an infinite FAC sheet.

### 3. Observations

#### 3.1. Interplanetary and Geomagnetic Conditions

Figure 1a shows a 1-day overview of IMF conditions on October 29, 2005. We note that the vector magnetic field (black, blue, and red lines for IMF  $B_x$ , IMF  $B_y$ , and IMF  $B_z$ , respectively) in geocentric solar

magnetospheric (GSM) coordinates and the corresponding IMF magnitude (thick magenta line for IMF  $B$ ) are plotted here. In addition to IMF  $B$ , the values of  $-IMF\ B$  are plotted here as a thin magenta line to show how close IMF  $B_x$  is to IMF  $B$  in magnitude. As shown in Figure 1a, IMF  $B_x$  was nearly constant ( $\sim -3.0$  nT), while IMF  $B_y$  ( $\sim -0.9$ – $2.1$  nT) and IMF  $B_z$  ( $\sim -2.1$ – $1.0$  nT) were varying during  $\sim 04:00$ – $16:00$  UT. However, the values in  $-IMF\ B$  are similar to those in IMF  $B_x$  during most of this interval, implying radially (earthward) oriented IMF. In order to determine the radial IMF condition, we calculate and plot the IMF  $B_x$  to IMF  $B$  ratio ( $IMF\ B_x / IMF\ B$ ) in Figure 1b. The red horizontal dashed line at  $-0.9$  ( $0.9$ ), which corresponds to an angle of  $\sim 25.8^\circ$  between the IMF direction and the Sun–Earth line toward the Earth (Sun), represents the threshold for the earthward (sunward) IMF condition (Neugebauer & Goldstein, 1997; Neugebauer et al., 1997; Park et al., 2016; Pi et al., 2014; Watari et al., 2005). We identify  $\sim 7$  hours from 08:22:30 to 15:37:30 UT (with  $\pm 2.5$  min uncertainties on either side) as a prolonged earthward IMF interval (marked by two vertical dashed lines) including a few isolated subintervals showing  $-0.9 < IMF\ B_x / IMF\ B \leq -0.8$  within 15 min (e.g.,  $IMF\ B_x / IMF\ B \sim -0.89$  at 09:27:30 UT). Overall, the  $IMF\ B_x / IMF\ B$  ratio is about  $-0.95$  (equivalent to an angle of  $\sim 18.3^\circ$  between the IMF direction and the Sun–Earth line toward the Earth) on average during this interval. Figures 1c and 1d show a monotonically decreasing solar wind speed (from  $\sim 390$  to  $\sim 360$  km/s) and increasing number density of protons (from  $\sim 4.4$  to  $\sim 10.0$  cm $^{-3}$ ) until 18:00 UT, which indicate that this prolonged radial IMF interval may be due to the passage of the trailing edge of a high-speed stream (Borovsky & Denton, 2016).

During this interval, the dipole tilt angle (Figure 1e) varied continuously from  $\sim -20^\circ$  to  $-4^\circ$ , which implies that the Earth's dipole axis was becoming approximately perpendicular to the Sun–Earth line. Therefore, the dipole tilt angle has minor effect on north-south hemispheric asymmetries in the lobe cell convection (Crooker & Rich, 1993) and in the ionospheric conductivity (Kullen et al., 2008; Østgaard et al., 2003; Reidy et al., 2018). The AL and AU indices, which are derived from ground magnetometer observatories located on average on the northern auroral oval (Davis & Sugiura, 1966), show nonsubstorm conditions (with  $\sim -50 < AL < 0$  nT and  $AU = \sim 50$  nT, except for the beginning of the radial IMF interval) during this interval (see Figure 1f), even though the IMF was sometimes weakly southward (see Figure 1b). After 15:37:30 UT, the AL index sharply decreased ( $AL < -400$  nT) with increasing  $IMF\ B_x / IMF\ B$  (up to  $-0.29$ ) under southward IMF conditions. These observations indicate quiet geomagnetic conditions during the prolonged radial IMF interval (Wang et al., 2014).

### 3.2. Auroral Emissions

Figures 2 and 3 show the cross-track scanned images of LBHS emissions in the northern and southern polar regions (poleward of  $\pm 60^\circ$  MLAT), respectively, measured by the TIMED/GUVI and DMSP F16/SSUSI around 10:30–15:00 UT on October 29, 2005. The time interval and the satellite for each image are denoted at the top of the corresponding figure. All images shown in Figures 2 and 3 are displayed in the MLAT–MLT frame of Altitude-Adjusted Corrected Geomagnetic (AACGM) coordinates (Baker & Wing, 1989; Shepherd, 2014). The concentric dashed circles represent constant MLATs at  $10^\circ$  intervals centered at  $\pm 90^\circ$  AACGM latitude. We note that during the period of interest, the TIMED/GUVI (DMSP F16/SSUSI) provided cross-track scanned images in approximately the postnoon–postmidnight (prenoon–premidnight) local time sector, which corresponds to its orbit direction. For each hemisphere, neighboring images have  $\sim 40$ – $60$  min time difference because these low-Earth orbiting satellites (with altitudes of  $\sim 840$  km for the DMSP F16 satellite and  $\sim 610$  km for the TIMED satellite) were traversing the polar regions in opposite hemispheres with orbital periods of  $\sim 100$  min. Figures 2 and 3 show that the auroral ovals in the northern and southern hemispheres were displaced a few degrees toward the midnight meridian with  $\sim \pm 70^\circ$  MLAT at night and  $\sim \pm 80^\circ$  MLAT at noon over  $\sim 10:30$ – $15:00$  UT.

In the northern hemisphere, TIMED/GUVI observed a local emission peak at  $\sim 80^\circ$  MLAT on the dawnside ( $\sim 0500$  MLT) of the polar cap at 10:27–10:46 UT (Figure 2a). However, it is not clear whether this structure is an isolated emission peak in the polar cap, a local emission peak inside the dawnside oval or the part of a TPA. This structure is hardly seen in the following DMSP F16/SSUSI image (Figure 2b). As shown in Figures 2c and 2e, TIMED/GUVI subsequently observed two clear TPAs (identified even by visual inspection): one TPA ( $\sim 1$  kR in radiance) located near the dawnside oval ( $\sim 80^\circ$  MLAT at 0600 MLT) and another



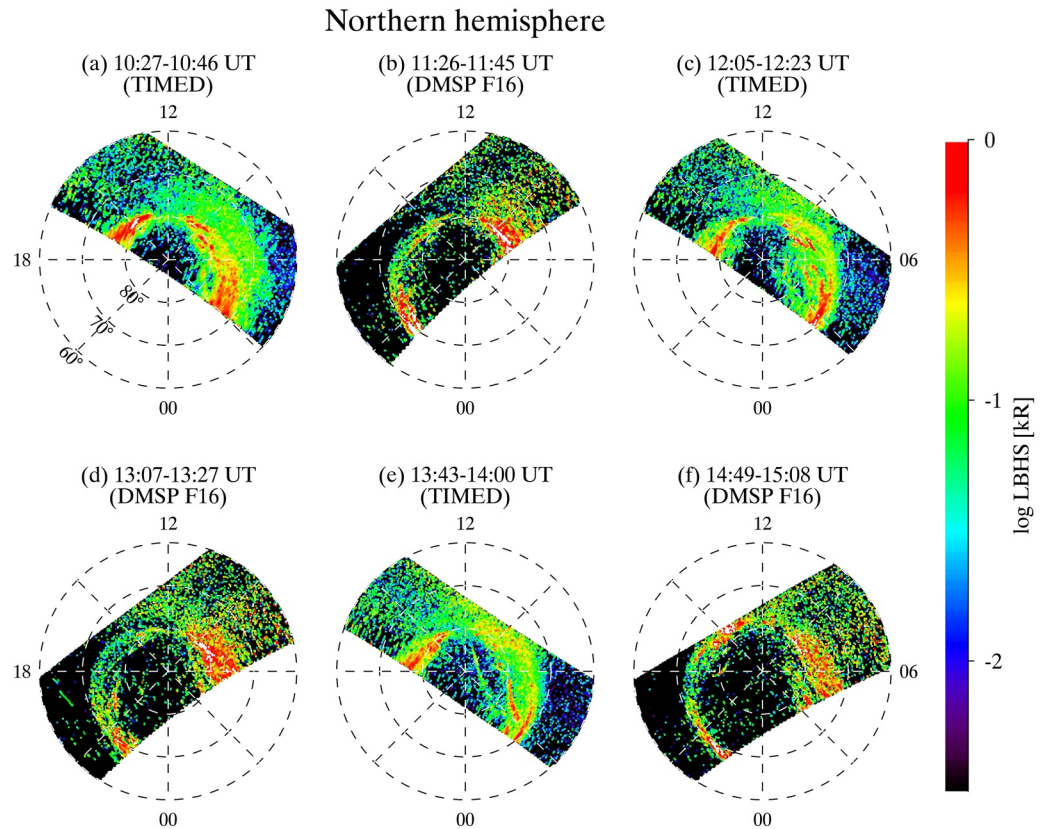


**Figure 2.** Cross-track scanned images of Lyman-Birge-Hopfield short (LBHS) emissions measured by Thermosphere Ionosphere Mesosphere Energetics and Dynamics (TIMED)/Global Ultraviolet Imager (GUVI) and Defense Meteorological Satellite Program (DMSP) F16/Special Sensor Ultraviolet Spectrographic Imager (SSUSI) around 10:30–15:00 UT in the northern hemisphere (magnetic latitude [MLAT]  $\geq 60^\circ$ ). The time interval for each image is denoted at the top of corresponding figure.

TPA ( $\sim 0.1$  kR in radiance) located near the magnetic pole (poleward of  $\sim 85^\circ$  MLAT at 0600 MLT). DMSP F16/SSUSI observed the TPA near the dawnside oval, but it is hard to identify the TPA near the magnetic pole (Figures 2d and 2f). These are probably because of some differences between the two instruments (see section 2.1 of Knight et al., 2018). The auroral images in the southern hemisphere, on the other hand, show the auroral oval devoid of TPAs until  $\sim 12:00$  UT (Figures 3a and 3b). A clear TPA structure with radiance  $\sim 1$  kR appeared on the dawnside of the polar cap after that time (Figures 3c–3f). Therefore, Figures 2 and 3 show that these two satellites observed the clear TPAs in both hemispheres during  $\sim 12:00$ – $15:00$  UT. Although it is difficult to determine its northern hemisphere counterpart (the TPA near the magnetic pole or that near the dawnside oval), the auroral images shown in Figures 2 and 3 also reveal that TPAs can appear in both hemispheres even under prolonged radial IMF conditions. The cross-track scanned images of LBHL emissions show almost the same TPA structures in both hemispheres as the LBHS emissions, although the LBHL band is not as sensitive as the LBHS band to the FUV emissions in the TPAs (see Figures S1 and S2 in supporting information).

In Figure 4, we plot the location of bright emission regions (where the LBHS emission is greater than or equal to 0.1 kR) in the northern and southern hemispheres in order to examine how the TPAs in both hemispheres move with time. The location of the bright emission regions in the northern (Figures 4a–4d) and southern (Figures 4e–4h) hemispheres observed during  $\sim 12:00$ – $15:00$  UT (when the clear TPAs are observed in both hemispheres) is reproduced based on the auroral images shown in Figures 2c–2f and Figures 3c–3f, respectively. It is noted that in Figure 4, we only show bright emission regions poleward of  $\pm 70^\circ$  MLAT to focus on the movement of the TPAs with time. The time intervals denoted in Figures 4a–4h are therefore a bit (several minutes) different from those shown in Figures 2c–2f and 3c–3f. The concentric

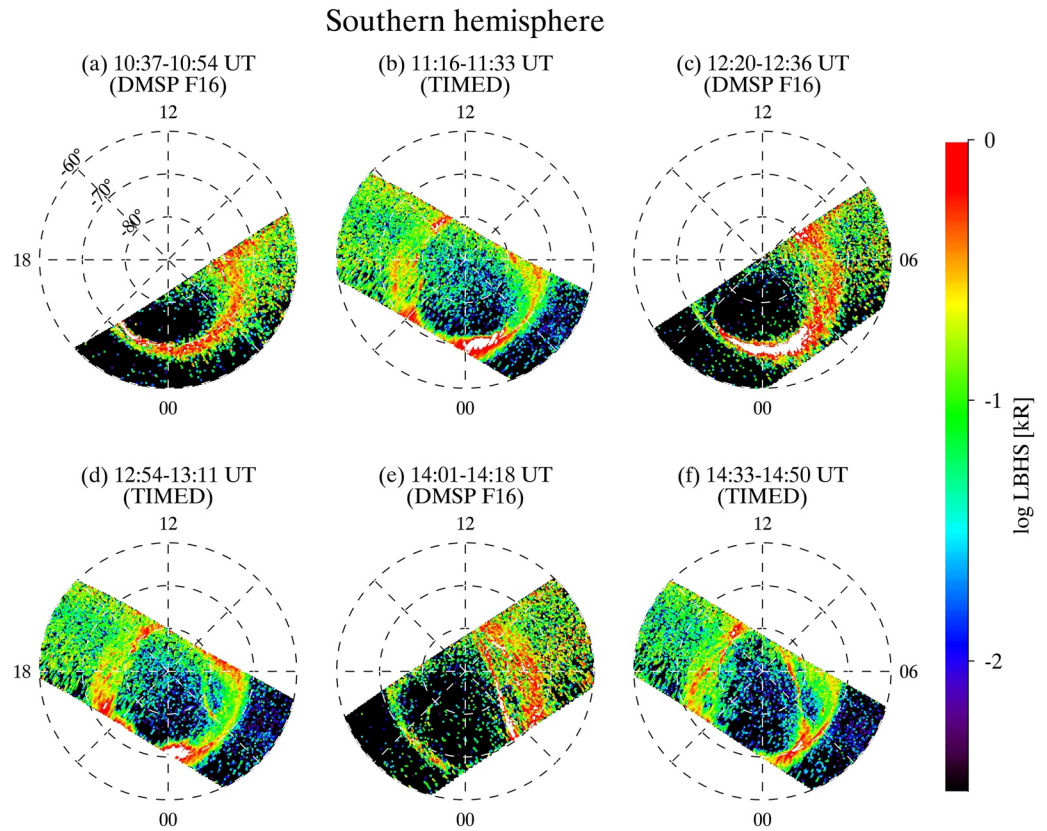


**Figure 3.** Same as Figure 2, but in the southern hemisphere (magnetic latitude [MLAT]  $\leq -60^\circ$ ).

dashed circles represent constant MLATs at  $5^\circ$  intervals. It is revealed from Figure 4 that during  $\sim 12:00$ – $15:00$  UT, the nightside parts of the southern hemisphere TPA and one of the northern hemisphere TPAs with radiance  $\sim 1$  kR (denoted by blue arrows) are likely to be connected to the auroral ovals in the post-midnight sector (located slightly later than 0300 MLT for the northern hemisphere one and slightly earlier than 0300 MLT for the southern hemisphere one) without any clear motion in MLT (less than  $\sim 1$  h MLT). The nightside part of the other northern hemisphere TPA with radiance  $\sim 0.1$  kR (denoted by red arrows in Figures 4a and 4c) is also likely to be connected to the auroral ovals in the postmidnight sector, but its MLT location is slightly earlier than 0300 MLT during the interval of interest.

### 3.3. Precipitating Particles, Plasma Flow, and Magnetic Perturbations

Figure 5 shows the DMSP F16 satellite pass (in AACGM coordinates) between 14:03 and 14:15 UT overplotted on the zoomed-in view (poleward of  $-70^\circ$  MLAT) of the corresponding auroral image (Figure 3e). The time interval for the auroral image is also denoted at the top of the figure. We note that the zoomed-in image is used to clearly show the satellite position with respect to the TPAs. The concentric dashed circles represent constant MLATs at  $5^\circ$  intervals centered at  $-90^\circ$  AACGM latitude. The white line and solid magenta arrowhead indicate the satellite track and the orbital direction, respectively. The satellite locations at 1-min intervals between 14:05 and 14:10 UT are represented by small circles. As shown in Figure 5, DMSP F16 passed through the southern hemisphere TPA (marked by the blue arrow) at  $\sim 14:08$  UT.

Figures 6a–6e show the differential energy flux spectrum for precipitating electrons, that for precipitating ions, integrated energy fluxes for these particle species, horizontal cross-track ion velocity, and residual cross-track magnetic field component (and estimated FAC density), respectively, observed by the DMSP F16 satellite at 14:05–14:10 UT. The satellite locations (MLAT and MLT in AACGM coordinates) are tabulated at the bottom of Figure 6e. Applying the definitions of Newell, Wing, et al. (1991) to interpret our data, Figure 6a shows that the transition region mapping between the central plasma sheet (characterized

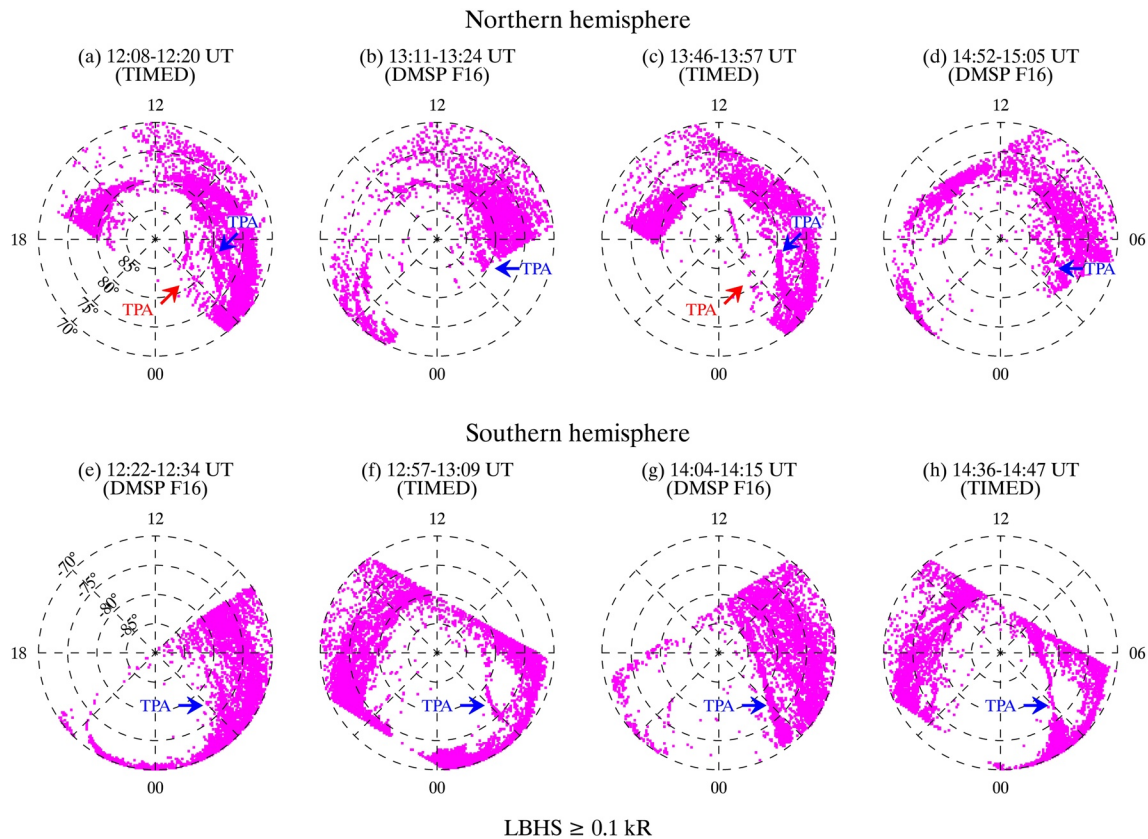


**Figure 4.** Location of the bright emission regions observed at magnetic latitudes (MLATs) poleward of  $\pm 70^\circ$  during  $\sim 12:00$ – $15:00$  UT. (a–d) In the northern hemisphere (plotted based on auroral images shown in Figures 2c–2f) and (e–h) in the southern hemisphere (plotted based on auroral images shown in Figures 3c–3f). The bright emission region is defined as the region where the Lyman-Birge-Hopfield short (LBHS) emission is greater than or equal to 0.1 kR. The blue and red arrows denote the TPAs, respectively, with radiances  $\sim 1$  and  $\sim 0.1$  kR.

by a few keV electrons) and the plasma sheet boundary layer (PSBL; characterized by tens of eV up to a few keV electrons) is located around  $-77^\circ$  MLAT ( $\sim 14:05:50$  UT). Precipitating ions with energies of a few keV and sunward flows at  $\sim 14:05:50$ – $14:06:30$  UT (shown in Figures 6b and 6d, respectively) are indicative of particles that originated in the PSBL (Newell, Burke, et al., 1991). Comparing Figures 6a and 6b, low-energy (up to a few hundred eV) electron precipitation without ions, called polar rain electrons (Winningham & Heikkila, 1974), can be seen in the southern polar cap (poleward of  $\sim -81^\circ$  MLAT).

Interestingly, Figures 6a and 6b show that the DMSP F16 satellite observed  $\sim 1$ – $10$  keV ions accompanied by the precipitation of electrons (with energies up to a few keV) at  $\sim 14:07:45$ – $14:08:10$  UT (denoted by the blue bar between Figures 6a and 6b), when this satellite passes through the southern hemisphere TPA (see the satellite position denoted by the blue bar in Figure 5). Figure 6c also shows that in this region (marked by two vertical dashed lines), the integrated energy fluxes for both particle species are elevated (up to  $\sim 10^{10}$ – $10^{12}$  eV/cm<sup>2</sup> s sr for electrons and  $\sim 10^{10}$  eV/cm<sup>2</sup> s sr for ions) compared to its surroundings (specifically,  $\sim 10^9$ – $10^{10}$  eV/cm<sup>2</sup> s sr for electrons and  $\sim 10^9$  eV/cm<sup>2</sup> s sr for ions at MLATs poleward of the TPA). These observations indicate that the southern hemisphere TPA is associated with particle (both electrons and ions) precipitation. The precipitating particles observed in this region are comparable in their energy range with those originating in the PSBL (see Figures 6a and 6b), although the differential energy flux spectrum for precipitating electrons shows an inverted-V structure at  $14:07:50$  UT. Figures 6a and 6b also show precipitating electrons and ions at  $\sim 14:07:20$ – $14:07:30$  UT and at  $\sim 14:08:45$ – $14:09:10$  UT. However, it is difficult to identify the corresponding TPAs in Figure 5. This is due probably to insufficient data quality to distinguish the TPA from the auroral oval (in the first interval) or low TPA intensity to be detected by the FUV instruments or the small-scale sizes to be identified as TPAs (in the second interval).



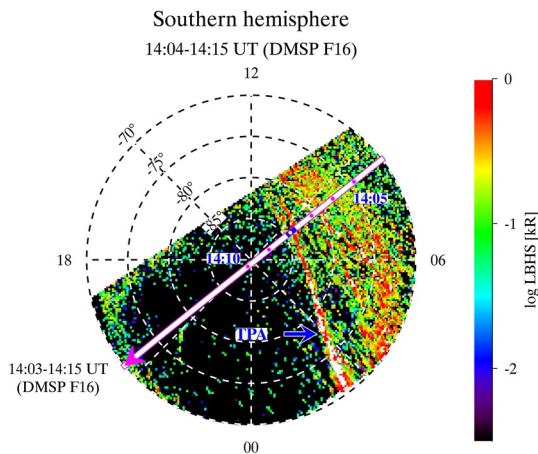


**Figure 5.** Southern hemisphere Defense Meteorological Satellite Program (DMSP) F16 satellite pass (in the magnetic latitude [MLAT]-magnetic local time [MLT] frame of Altitude-Adjusted Corrected Geomagnetic [AACGM] coordinates) between 14:03 and 14:15 UT (white line with solid magenta arrowhead) overplotted on the zoomed-in view (poleward of  $-70^\circ$  MLAT) of Figure 3e (an auroral image taken by DMSP F16/Special Sensor Ultraviolet Spectrographic Imager [SSUSI] at 14:04–14:15 UT). The small circles on the white line represent the satellite positions at 1-min intervals between 14:05 and 14:10 UT. The blue bar on the white line indicates the position of the DMSP F16 satellite during 14:07:45–14:08:10 UT (see text for details). The transpolar arc (TPA) with radiances  $\sim 1$  kR is marked by the blue arrow.

The horizontal cross-track ion velocity data flagged as “good” and “caution” (black and orange circles, respectively, in Figure 6d) indicate the existence of sunward plasma flows (with magnitude up to  $\sim 600$  m/s) in most regions across the alignment of the southern hemisphere TPA (also marked by two vertical dashed lines). Moreover, they show flow shears with antisunward flows (maximum  $\sim 1,100$  m/s in magnitude) on dawn-side of the TPA and sunward flows (maximum  $\sim 600$  m/s in magnitude) on dusk-side of it. Because the satellite track is approximately orthogonal to the alignment of the southern hemisphere TPA (see Figure 5), the flow shears shown in Figure 6d (varying from antisunward to sunward along the dawn-to-dusk satellite pass) are suggestive of an upward FAC region with converging electric field structure (e.g., Lyons, 1980).

In Figure 6e, the residual cross-track magnetic field component (at 1-s cadence) along the satellite track at 14:05–14:10 UT is denoted by the thin black line. The noise-like structures in the residual cross-track magnetic field component are smoothed by applying 7-s (which corresponds to  $\sim 50$  km in the spatial scale) running averages (denoted by the thick black line) to the 1-s cadence data. The FAC density estimated using Equation 1 with the running-averaged data is also plotted as the red line in Figure 6e. We note that positive (negative) values of the FAC density correspond to upward (downward) FACs (that is,  $j_{\parallel} = -j_x$ ). It is obvious from the FAC density profile that an upward FAC system (positive  $j_{\parallel}$  region) exists in general in the southern hemisphere TPA (on the equatorward portion at  $\sim 14:07:50$ – $14:08:00$  UT and on the poleward portion around 14:08:05 UT), which is generally consistent with the direction of the FACs estimated from the horizontal cross-track ion velocity data (Figure 6d).

Unfortunately, there are no detectors for precipitating particles, plasma drift velocity, and magnetic field on the TIMED satellite. Moreover, the DMSP F16 satellite orbited the postdusk-to-prenoon MLT sectors and passed close to the auroral oval near noon MLT in the northern hemisphere during intervals presented in Figures 2d and 2f (also see Figures S3 and S4 in supporting information, respectively, for more details). Therefore, we cannot use DMSP F16 observations to examine the characteristics of the particle precipitation and plasma flow in the TPA regions in the northern hemisphere. However, the DMSP F13 satellite orbited the dusk-to-postdawn MLT sectors in the northern hemisphere. Figure 7 shows the DMSP F13 satellite pass between 14:33 and 14:45 UT overplotted on the zoomed-in view (poleward of  $70^\circ$  MLAT) of Figure 2e (an auroral image taken by TIMED/GUVI at 13:46–13:57 UT). The format of Figure 7 is the same as Figure 5, except that the concentric dashed circles represent constant MLATs at  $5^\circ$  intervals centered at  $90^\circ$  AACGM latitude. The DMSP F13 positions at 1-min intervals between 14:40 and 14:45 UT are denoted by small circles on the satellite pass, and the TPA with radiance  $\sim 0.1$  kR ( $\sim 1$  kR) is marked by the red (blue) arrow. Figure 7 shows that the DMSP F13 satellite passed through the TPA near the northern magnetic pole between 14:40 and 14:41 UT, under the assumption that the TPA marked by the red arrow is a stationary arc, but not seen in Figure 2f (the closest in time to the DMSP F13 satellite pass shown in Figure 7) due to some differences between DMSP F16/SSUSI and TIMED/GUVI instruments.

Figures 8a–8c show the differential energy flux spectra for precipitating electrons and ions and their integrated energy fluxes, respectively, observed by the DMSP F13 satellite during 14:40–14:45 UT. It can be seen from Figures 8a and 8b that the DMSP F13 satellite detected precipitating electrons (with energies up to a few hundred eV) without clear signatures of ion precipitation between  $\sim 14:40:25$  and  $14:40:40$  UT (marked by the red bar between Figures 8a and 8b), when this satellite was located close to the TPA near the northern magnetic pole (see the satellite position denoted by the red bar in Figure 7). Figure 8c also shows that during this time (marked by two dotted vertical lines), the integrated energy flux for precipitating electrons (black line) is generally higher by a factor of  $\sim 100$  ( $\sim 10^{10}$  eV/cm<sup>2</sup> s sr) compared to before and after this interval ( $\sim 10^8$  eV/cm<sup>2</sup> s sr), while that for precipitating ions (red line) is overall comparable in magnitude to its surroundings (typically in the order of  $10^7$ – $10^9$  eV/cm<sup>2</sup> s sr). These observations indicate that the TPA near

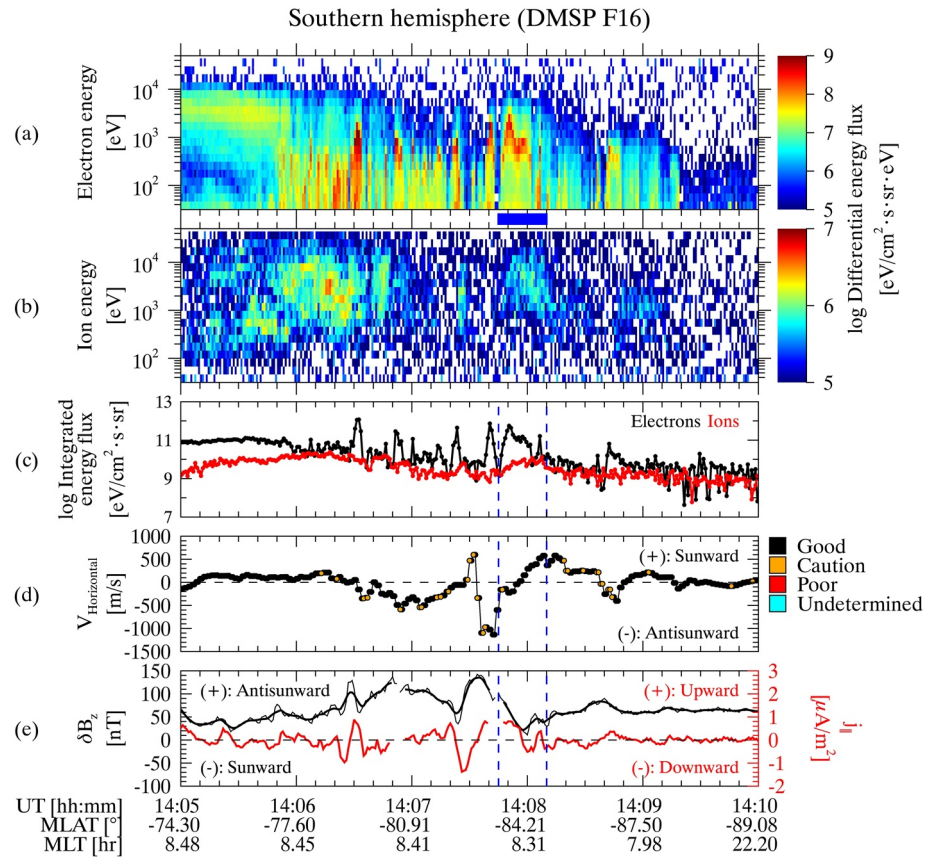


**Figure 6.** Defense Meteorological Satellite Program (DMSP) F16 observations at 14:05–14:10 UT. (a) Differential energy flux spectrum for precipitating electrons, (b) differential energy flux spectrum for precipitating ions, (c) integrated energy flux for precipitating electrons (black) and ions (red), (d) horizontal cross-track ion velocity, and (e) cross-track residual magnetic field component (thin black line for 1-s cadence data and thick black line for their 7-s running averages) and corresponding FACs (thick red line) are plotted. The horizontal cross-track ion velocity data in Figure 6d are color-coded based on their quality flags (black being “good”, orange being “caution”, red being “poor”, and aqua being “undetermined”). The blue bar between Figures 6a and 6b and the corresponding two vertical dashed lines in Figures 6c–6e indicate the transpolar arc (TPA)-associated particle (both electrons and ions) precipitation region observed during 14:07:45–14:08:10 UT.

the northern magnetic pole is associated with electron-only precipitation. The horizontal cross-track ion velocity data flagged as “good” and “caution” (black and orange circles in Figure 8d) show antisunward flows (maximum  $\sim 500$  m/s in magnitude) in the electron-only precipitation region (also marked by two dotted vertical lines), compared to background conditions (antisunward flows with magnitude  $\sim 100$ – $200$  m/s). The data marked with “undetermined” (aqua circles) also show antisunward flows (with magnitude  $\sim 500$  m/s) at  $\sim 14:40:40$  UT. This provides more evidence for the existence of strong antisunward flows in the TPA near the northern magnetic pole (compared to its surroundings).

In addition to the electron-only precipitation, the DMSP F13 satellite observed both ion (with energies of a few keV) and electron (with energies up to  $\sim 1$  keV) precipitation at  $\sim 14:41:25$ – $14:41:45$  UT and at  $\sim 14:41:55$ – $14:42:15$  UT (denoted by two blue bars between Figures 8a and 8b and four vertical dashed lines in Figures 8c–8e). Both precipitating electrons and ions observed in these intervals are comparable in energy range with those observed at  $\sim 14:43:00$ – $14:43:50$  UT. The integrated energy flux for both electrons and ions (Figure 8c) is higher during this time interval (in the order of  $10^9$ – $10^{11}$  eV/cm<sup>2</sup> s sr for electrons and in the order of  $10^9$  eV/cm<sup>2</sup> s sr for ions, respectively) compared to before and after the interval (typically  $\sim 10^8$ – $10^9$  eV/cm<sup>2</sup> s sr for both electrons and ions). Figure 8d also shows the existence of sunward plasma flows (with magnitude up to  $\sim 600$  m/s), which are surrounded by antisunward flows (with magnitude up to a few hundred m/s). Moreover, flow shears from sunward to antisunward along the dusk-to-dawn satellite

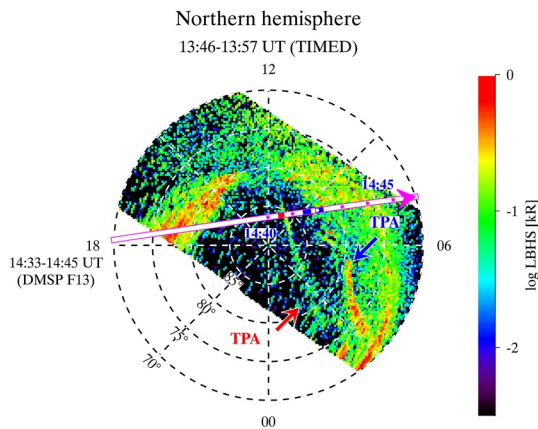


**Figure 7.** Same as Figure 5, but northern hemisphere Defense Meteorological Satellite Program (DMSP) F13 satellite pass between 14:33 and 14:45 UT overplotted on the zoomed-in view (poleward of  $70^\circ$  magnetic latitude [MLAT]) of Figure 2e (an auroral image taken by Thermosphere Ionosphere Mesosphere Energetics and Dynamics [TIMED]/Global Ultraviolet Imager [GUVI] at 13:46–13:57 UT). The small circles on the white line represent the satellite positions at 1-min intervals between 14:40 and 14:45 UT. The red bar and two blue bars on the white line indicate the DMSP F13 satellite positions during 14:40:25–14:40:40 UT, 14:41:25–14:41:45 UT, and 14:41:55–14:42:15 UT, respectively (see text for details). The transpolar arc (TPA) with radiances  $\sim 0.1$  kR ( $\sim 1$  kR) is marked by the red (blue) arrow.

pass (implying upward FACs with converging electric field structures) can be seen in each of the precipitation regions. Although these precipitating particles/plasma flow properties are not collocated with the TPA marked by the blue arrow in Figure 7, they are located in the TPA shown in Figure 2d (also see supporting information Figure S3), or close to the TPA shown in Figure 2f (also see supporting information Figure S4). This is in agreement with our observation that the northern hemisphere TPA near the dawnside oval (denoted by the blue arrow in Figures 4a–4d) is the stationary one, although this structure is not clearly distinguishable in the TIMED/GUVI image (Figure 7).

As shown in Figure 8e, the FAC density profile along the satellite track (red line) also indicates the existence of an upward FAC system in the northern hemisphere TPA near the dawnside oval. However, it is difficult to determine the FAC system on the TPA near the northern magnetic pole because of the data gap in the magnetic field measurements at  $\sim 14:40:30$  UT. We also note that although the FAC density is estimated using the low-pass filtered magnetic field data (that is, 7-s running averages of  $\delta B_z$ ), there are fluctuations in the FAC density profile due to noise-like structure in the residual cross-track magnetic field component obtained from the DMSP F13 observations (thin black line).

#### 4. Discussion

In this study, we have presented TPAs observed during a prolonged radial IMF interval on October 29, 2005. The IMF  $B_x$  / IMF  $B_z$  ratio (Figure 1b) is about  $-0.95$  on average during 08:22:30–15:37:30 UT, equivalent to an

angle of  $\sim 18.3^\circ$  between the IMF direction and the Sun–Earth line toward the Earth. During this period, low-Earth orbiting DMSP F16 and TIMED satellites were located in opposite polar regions. Therefore, FUV emission measurements from these satellites provide a good opportunity for an interhemispheric study of TPAs in response to the IMF orientation.

Fear and Milan (2012) observed that the MLT at which the TPA first forms is generally dependent on the IMF  $B_y$  orientation that affects the dawn-dusk component of the magnetic field in the magnetotail adjacent to the plasma sheet. In the presence of IMF  $B_y$  under northward IMF conditions, magnetic reconnection between distorted tail field lines (Grocott et al., 2004, 2005) is responsible for the protrusion of closed field lines into the tail lobes to form the TPAs mirrored about the noon-midnight meridian between hemispheres (Milan et al., 2005). In the present event, however, the cross-track scanned images of auroral emissions (Figures 2 and 3) show that TPAs with a radiance of  $\sim 1$  kR are observed near the dawnside ovals in both hemispheres during  $\sim 12:00$ – $15:00$  UT. Moreover, the AL and AU indices (Figure 1f) indicate nonsubstorm conditions (with  $\sim -50 < \text{AL} < 0$  nT and  $\text{AU} = \sim 50$  nT) during this period regardless of the IMF  $B_z$  orientation (see Figure 1a), implying that the IMF  $B_z$  orientation does not significantly affect geomagnetic activity. Based on these observations, we speculate that the IMF  $B_z$  as well as the IMF  $B_y$  impinging on the Earth's bow shock does not act significantly on the formation the TPAs presented here.

Grocott (2017) pointed out that the location of newly closed field lines in the plasma sheet would be offset toward the dawn sector under dawnward IMF conditions on a long timescale (tens of hours). However, IMF pointed duskward over much of the 1-day interval prior to the onset of the clear TPAs in both polar caps except a few subintervals including  $\sim 01:00$ – $04:00$  UT interval shown in Figure 1 (IMF  $B_y$  on October 28–29, 2005 is shown in supporting information Figure S5). Moreover, we have shown that the satellites observed the clear TPAs in both hemispheres during  $\sim 12:00$ – $15:00$  UT (Figures 2c–2f and 3c–3f). The start time of these TPA observations is therefore  $\sim 3$ – $4$  h after the onset time of earthward IMF conditions (08:22:30 UT), which is comparable to the response time of TPAs to the IMF orientation (Fear & Milan, 2012). These imply that the formation mechanism for our TPA event is independent of the IMF orientation prior to the prolonged earthward IMF interval.



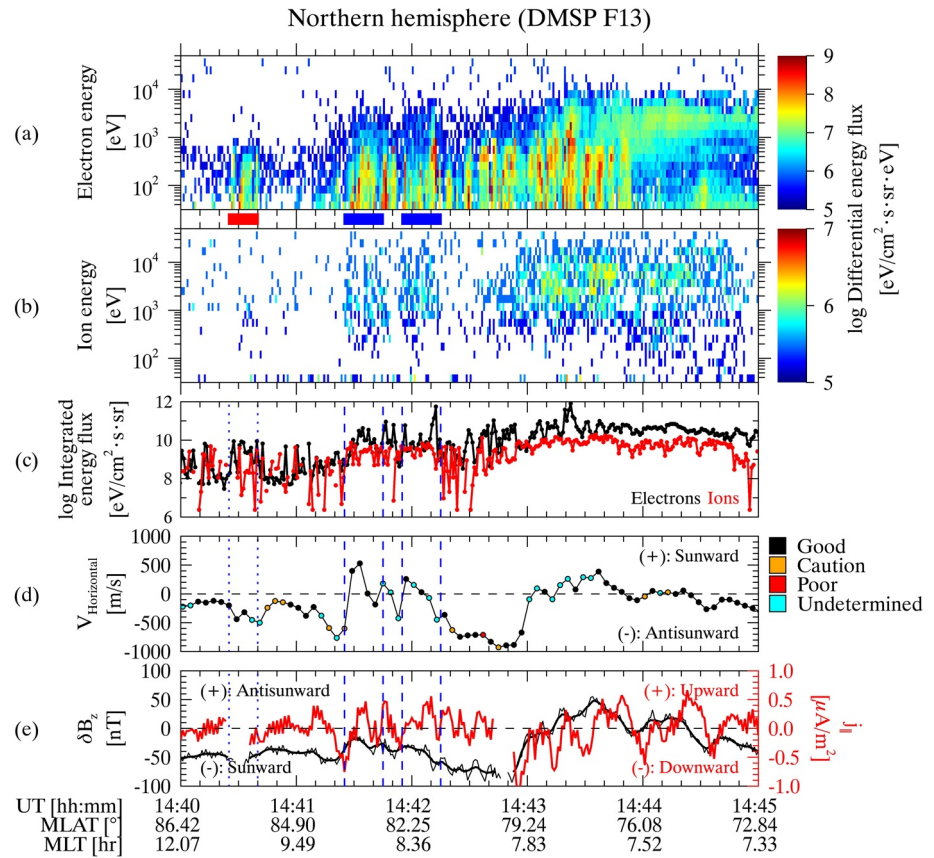


**Figure 8.** Same as Figure 6, but Defense Meteorological Satellite Program (DMSP) F13 observations at 14:40–14:45 UT. Two blue bars and the corresponding four vertical dashed lines (at 14:41:25–14:41:45 UT and 14:41:55–14:42:15 UT) indicate the transpolar arc (TPA)-associated particle (both electrons and ions) precipitation regions, while the red bar and the corresponding two vertical dotted lines (at 14:40:25–14:40:40 UT) indicate the TPA-associated electron-only precipitation region.

Based on our observational results, we propose the following terrestrial magnetic field configuration connected to the TPAs during the interval of interest. Figure 9 presents a schematic illustration of the noon-midnight meridional cross-section of the terrestrial magnetic field configuration (not to the scale) under earthward IMF conditions. We note that a purely earthward IMF and  $0^\circ$  in dipole tilt angle are adopted here for simplicity. Because of the draping effect of the radially oriented IMF (Petrinec, 2016; Pi et al., 2017), the earthward-directed IMF is plotted to drape over the magnetopause, so that the southward draped field lines lead to magnetic reconnection with oppositely directed terrestrial magnetic field lines sunward of the southern cusp region. Consequently, the reconnected field lines are open, and their ionospheric footprints are located in both the northern and southern hemispheres. On the other hand, the northward draped field lines cause magnetic reconnection tailward of the northern cusp region. Although the field lines which are reconnected on the tailward side of the northern cusp are also open, their ionospheric footprints are in the northern hemisphere only. This implies that the northward draped IMF is exerted mainly in the northern hemisphere.

The presence of electrons and ions that precipitate into the TPAs in both hemispheres is considered as a proxy of a closed field line configuration (Carter et al., 2017; Fear et al., 2014; Reidy et al., 2017, 2018; Xing et al., 2018). Previous studies pointed out that not only magnetic reconnection (Fear & Milan, 2012; Milan et al., 2005; Nowada et al., 2018), strong plasma flow shears that cause pairs of FACs (Nowada et al., 2020; Q.-H. Zhang et al., 2020), and the ballooning instability (Golovchanskaya et al., 2006; Rezhnevov, 1995) in the magnetotail but also the Kelvin-Helmholtz instability (Y. Zhang et al., 2016; Q.-H. Zhang et al., 2020) and the interchange instability (Kozlovsky et al., 2007) on the flankside magnetopause can be considered as



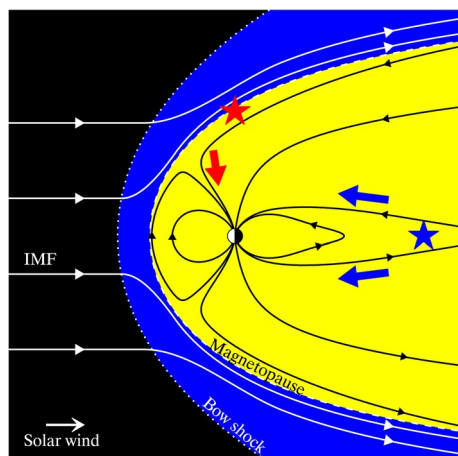


**Figure 9.** Schematic illustration (not to the scale) of the terrestrial magnetic field configuration (in the noon-midnight meridional plane) with  $0^\circ$  in dipole tilt angle under purely earthward interplanetary magnetic field (IMF) conditions. Two “star” symbols denote the potential regions associated with the precipitating particles on closed (blue) and open (red) field lines: in the magnetotail and on the northern nightside magnetopause, respectively. The thick arrows in blue and red represent the motions of precipitating particles, respectively, on closed and open field lines.

generation mechanisms for TPAs on closed field lines. In these scenarios, the candidate sources on the flank magnetopause cause the TPAs in both hemispheres to continually drift in MLT toward midnight as the source region drifts tailward with the solar wind flow. This is inconsistent with our observations that the TPAs in both hemispheres remained within 1 h MLT of  $\sim 0300$  MLT during  $\sim 12:00$ – $15:00$  UT (see Figure 4). Therefore, we suggest that the precipitating particles that cause the TPAs in the dawn sector of the polar caps are from the magnetotail, rather than from the flank magnetopause. Moreover, the differential energy flux spectra for the precipitating particles above these TPAs show similar properties in their energy range to those above the main auroral oval (see Figures 6a, 6b and , 8a and 8b). These TPAs are flanked on both sides by polar rain type fluxes with antisunward flows (with respect to those in the TPAs). The mostly sunward flows (Figures 6d and 8d) and upward FACs (Figures 6e and 8e) observed during the TPA crossings also support our suggestion that the source region for these TPA structures is in the magnetotail, such as the PSBL (Newell, Burke, et al., 1991). However, it is unclear whether particle precipitation along “newly” closed field lines by magnetic reconnection in the magnetotail (e.g., Fear et al., 2015; Milan et al., 2005) or along “already” closed field lines extruded from the plasma sheet into the tail lobes (e.g., Huang et al., 1987; Kullen, 2012) leads to the formation of the observed TPAs. The blue star symbol and the thick arrows in Figure 9 correspond to the potential region (in the magnetotail) and the motions of the precipitating particles, respectively, associated with the closed field

line scenario. By applying the terrestrial magnetic field configuration shown in Figure 9 to our observation (the TPAs on closed field lines in both hemispheres under earthward IMF conditions), we also suggest that the TPA formation is not limited to northward IMF conditions.

If the TPA is on open field lines connected directly to the northward draped IMF, this arc structure would occur in one hemisphere where magnetic reconnection tailward of the cusp takes place. We speculate that the occurrence of the TPA with radiance  $\sim 0.1$  kR near the northern magnetic pole (shown in Figures 2c and 2e) is associated with magnetic reconnection tailward of the cusp under the earthward-directed IMF. The magnetic reconnection tailward of the northern cusp region produces a low-latitude boundary layer in the northern hemisphere, and the consequent field lines in the outer part of this region are open (Pi et al., 2018; Tang et al., 2013). These imply that electron-only precipitation (so called type B polar showers), which is on open field lines and originates in solar wind electrons, can occur more frequently in the northern hemisphere polar cap (Shinohara & Kokubun, 1996). This is consistent with our observations that the electron-only precipitation region at  $\sim 14:40:25$ – $14:40:40$  UT (shown in Figures 8a–8c) is close to the TPA with radiance  $\sim 0.1$  kR near the northern magnetic pole, under the assumption that the TPA in Figure 2e (also see Figure 7) is the stationary one, but not seen in Figure 2f (also see Figure S4 in supporting information) due to the differences between DMSP F16/SSUSI and TIMED/GUVI instruments. Therefore, we suggest that the TPA with radiance  $\sim 0.1$  kR near the northern magnetic pole is formed by accelerated polar rain electrons occurring on open field lines (Carlson & Cowley, 2005; Newell et al., 2009; Reidy et al., 2017, 2018). The red star symbol and the thick arrow in Figure 9 show the potential region (tailward side of the cusp) and the motion of precipitating electrons, respectively, associated with the open field line scenario under earthward IMF conditions.

We note that it is unclear how the TPA on open field lines is extended to the nightside polar cap under radial IMF conditions. Song et al. (1999) showed using global magnetohydrodynamic (MHD) simulations that the antisunward convection region in the polar caps is on closed field lines (except in the cusps) under purely northward IMF conditions. According to their result, the newly closed field lines on the dayside, which are generated by magnetic reconnection on the tailward side of the cusps, convect antisunward along the magnetopause with trapped solar wind plasma. Their ionospheric footprints are within the polar caps and move to the midnight along both sides of them. The footprints of these field lines eventually return to the dayside through the polar caps as the magnetospheric flow moves further away from the Earth.

If the IMF  $B_x$  component is nonzero, however, the reconnected field lines may be open (Song et al., 1999). We speculate that the TPA with radiance  $\sim 0.1$  kR near the northern magnetic pole, which is associated with the electron-only precipitation and the antisunward flow, is likely on the ionospheric footprint of the open field lines (generated by magnetic reconnection on the tailward side of the northern cusp) dragged tailward by the solar wind flow. Kan and Burke (1985) suggested that the arc structure on open field lines occurs in the region of antisunward ionospheric flow in the dawn sector of the polar caps under the assumption that such structure must be located in the upward FAC region. This is consistent with our observations that the northern hemisphere TPA with radiance  $\sim 0.1$  kR (marked by the red arrow in Figure 7) is located close to the antisunward flow region (see Figure 8d) in the dawn sector with respect to the noon-midnight meridian. However, further studies (e.g., dealing with the global ionospheric convection pattern in the vicinity of the observed TPAs) are required to understand the physical mechanisms under these conditions.

In this study, we have proposed the magnetic field topology connected to the TPAs (open or closed field lines) based on the characteristics of the precipitating particles, horizontal cross-track ion velocity, and cross-track magnetic field component (and the corresponding FAC density) observed when the DMSP satellites passed through the TPA regions. Therefore, our interpretation is only strictly valid within a localized region in the vicinity of the DMSP satellite as it passes above the TPAs, and not necessarily along the entirety of the TPA structure in the ionosphere, as pointed out by Y. Zhang et al. (2016). However, it does not affect our conclusions that TPA formation is not limited to northward IMF conditions and TPAs can occur on both closed and open field lines. The studies of the characteristics of the precipitating particles, plasma drift velocity, and FAC system along an entire TPA will provide more evidence for various mechanisms that form the TPA and the corresponding magnetic field configuration connecting the TPA with its source region. The large-scale plasma convection pattern in the polar ionosphere could be deduced from the line-of-sight velocity observations via Super Dual Auroral Radar Network (SuperDARN) array of high-frequency radars (Greenwald et al., 1995). Unfortunately, there is no relevant SuperDARN line-of-sight velocity data near the TPA regions during the interval of interest (not shown), and we leave the plasma convection pattern in both hemispheres during prolonged radial IMF intervals and its association with the TPAs as further studies.

## 5. Conclusions

For several decades, many studies have contributed to understanding how solar wind energy enters the magnetosphere and penetrates to the ionosphere when the IMF is parallel/antiparallel to the Earth's magnetic dipole moment (Dungey, 1961, 1963; Song & Vasyliūnas, 2010). In this study, we have turned our attention to the solar wind-magnetosphere-ionosphere coupling under radial IMF conditions, via TPA observations. Our observational results have revealed that TPA formation is not limited to northward IMF conditions. The TPAs presented here are associated with two distinct source regions that indicate widely different magnetic topologies. In one case, the TPA appears to be located on open field lines connected to the northward field lines draped over one hemisphere of the magnetopause, while in the other case the TPA appears to be located on closed field lines rooted in the polar cap of both hemispheres. In other words, the TPAs we observed are the result of both direct and indirect processes of solar wind energy transfer to localized regions in the high-latitude ionosphere.

## Data Availability Statement

DMSP F16/SSUSI data were obtained from <https://ssusi.jhuapl.edu/>. TIMED/GUVI data are available at <http://guvitimed.jhuapl.edu/>. DMSP/SSJ data were obtained from <https://www.ngdc.noaa.gov/stp/satellite/dmsp/>. DMSP/SSIES and DMSP/SSM data are accessible from the Madrigal database (<http://cedar.openmadrigal.org/>). The coefficients and software used to transform the DMSP satellite position from geographic (obtained from <https://sscweb.gsfc.nasa.gov/cgi-bin/Locator.cgi>) into AACGM coordinates are downloadable at <http://superdarn.thayer.dartmouth.edu/aacgm.html>. OMNI data were obtained from <https://omniweb.gsfc.nasa.gov/>. The software used to obtain the Earth's dipole tilt angle is downloadable at [http://ampere.jhuapl.edu/code/idl\\_geopack.html](http://ampere.jhuapl.edu/code/idl_geopack.html). AL and AU indices were obtained from <http://wdc.kugi.kyoto-u.ac.jp/>.

## Acknowledgments

This work was supported by NSFC grant 41850410495. Q. Q. Shi is supported by NSFC grants 41974189 and 41961130382 and the Royal Society NAF/R1/191047. M. Nowada is supported by NSFC grant 42074194. The work of K.-H. Kim was supported by the Basic Science Research Program through NRF funded by NRF-2019R1F1A1055444. A. M. Tian is supported by the Shandong University (Weihai) Future Plan for Young Scholars (2017WHWLJH08). T. Pitkanen was supported by NSFC grant 41750110486 and SNSA grant 118/17. I. J. Rae is supported in part by STFC grants ST/N0007722/1 and ST/S000240/1 and NERC grants NE/P017150/1 and NE/P017185/1. The authors wish to thank the International Space Science Institute in Beijing (ISSI-BJ) for supporting and hosting the meetings of the International Team on "The morphology of auroras at Earth and giant planets: characteristics and their magnetospheric implications", during which the discussions leading/contributing to this publication were initiated/held.

## References

- Baker, K. B., & Wing, S. (1989). A new magnetic coordinate system for conjugate studies at high latitudes. *Journal of Geophysical Research*, 94(A7), 9139–9143. <https://doi.org/10.1029/JA094iA07p09139>
- Berkey, F. T., & Kamide, Y. (1976). On the distribution of global auroras during intervals of magnetospheric quiet. *Journal of Geophysical Research*, 81(25), 4701–4714. <https://doi.org/10.1029/ja081i025p04701>
- Borovsky, J. E., & Denton, M. H. (2016). The trailing edges of high-speed streams at 1 AU. *Journal of Geophysical Research: Space Physics*, 121(7), 6107–6140. <https://doi.org/10.1002/2016JA022863>
- Carlson, H. C., & Cowley, S. W. H. (2005). Accelerated polar rain electrons as the source of Sun-aligned arcs in the polar cap during northward interplanetary magnetic field conditions. *Journal of Geophysical Research*, 110, A05302. <https://doi.org/10.1029/2004JA010669>
- Carter, J. A., Milan, S. E., Fear, R. C., Walach, M.-T., Harrison, Z. A., Paxton, L. J., & Hubert, B. (2017). Transpolar arcs observed simultaneously in both hemispheres. *Journal of Geophysical Research: Space Physics*, 122(6), 6107–6120. <https://doi.org/10.1002/2016JA023830>
- Christensen, A. B., Walterscheid, R. L., Ross, M. N., Meng, C.-I., Paxton, L. J., Anderson, D. E., et al. (1994). The Global Ultraviolet Imager (GUVI) for the NASA TIMED mission. In J. Wang, & P. B. Hays (Eds.), *Optical spectroscopic techniques and instrumentation for atmospheric and space research, proc. SPIE 2266* (pp. 451–466). Bellingham, Washington: SPIE. <https://doi.org/10.1117/12.187583>
- Crooker, N. U., & Rich, F. J. (1993). Lobe cell convection as a summer phenomenon. *Journal of Geophysical Research*, 98(A8), 13403–13407. <https://doi.org/10.1029/93JA01037>
- Davis, T. N., & Sugiura, M. (1966). Auroral electrojet activity index *AE* and its universal time variations. *Journal of Geophysical Research*, 71(3), 785–801. <https://doi.org/10.1029/JZ071i003p00785>
- Dungey, J. W. (1961). Interplanetary magnetic field and the auroral zones. *Physical Review Letters*, 6, 47–48. <https://doi.org/10.1103/PhysRevLett.6.47>
- Dungey, J. W. (1963). The structure of the exosphere, or adventures in velocity space. In C. De-Witt, J. Hiebolt, & A. Lebeau (Eds.), *Geophysics, the Earth's environment* (pp. 526–536). New York: Gordon and Breach.
- Farris, M. H., & Russell, C. T. (1994). Determining the standoff distance of the bow shock: Mach number dependence and use of models. *Journal of Geophysical Research*, 99(A9), 17681–17689. <https://doi.org/10.1029/94JA01020>
- Fear, R. C., & Milan, S. E. (2012). The IMF dependence of the local time of transpolar arcs: Implications for formation mechanism. *Journal of Geophysical Research*, 117, A03213. <https://doi.org/10.1029/2011JA017209>
- Fear, R. C., Milan, S. E., Carter, J. A., & Maggiolo, R. (2015). The interaction between transpolar arcs and cusp spots. *Geophysical Research Letters*, 42(22), 9685–9693. <https://doi.org/10.1002/2015GL066194>
- Fear, R. C., Milan, S. E., Maggiolo, R., Fazakerley, A. N., Dandouras, I., & Mende, S. B. (2014). Direct observation of closed magnetic flux trapped in the high-latitude magnetosphere. *Science*, 346(6216), 1506–1510. <https://doi.org/10.1126/science.1257377>
- Frank, L. A., Craven, J. D., Burch, J. L., & Winningham, J. D. (1982). Polar views of the Earth's aurora with Dynamics Explorer. *Geophysical Research Letters*, 9(9), 1001–1004. <https://doi.org/10.1029/GL009i009p01001>
- Golovchanskaya, I. V., Kullen, A., Maltsev, Y. P., & Biernat, H. (2006). Ballooning instability at the plasma sheet-lobe interface and its implications for polar arc formation. *Journal of Geophysical Research*, 111, A11216. <https://doi.org/10.1029/2005JA011092>
- Greenwald, R. A., Baker, K. B., Dudeney, J. R., Pinnock, M., Jones, T. B., Thomas, E. C., et al. (1995). DARN/SuperDARN: A global view of the dynamics of high-latitude convection. *Space Science Reviews*, 71, 761–796. <https://doi.org/10.1007/BF00751350>
- Grocott, A. (2017). Time-dependence of dawn-dusk asymmetries in the terrestrial ionospheric convection pattern. In S. Haaland, A. Runov, & C. Forsyth (Eds.), *Dawn-dusk asymmetries in planetary plasma environments, Geophysical Monograph Series* (pp. 107–123). Washington, DC: American Geophysical Union. <https://doi.org/10.1002/9781119216346.ch9>
- Grocott, A., Badman, S. V., Cowley, S. W. H., Yeoman, T. K., & Cripps, P. J. (2004). The influence of IMF By on the nature of the nightside high-latitude ionospheric flow during intervals of positive IMF Bz. *Annales Geophysicae*, 22(5), 1755–1764. <https://doi.org/10.5194/angeo-22-1755-2004>
- Grocott, A., Yeoman, T. K., Milan, S. E., & Cowley, S. W. H. (2005). Interhemispheric observations of the ionospheric signature of tail reconnection during IMF-northward non-substorm intervals. *Annales Geophysicae*, 23(5), 1763–1770. <https://doi.org/10.5194/angeo-23-1763-2005>
- Gusev, M. G., & Troshichev, O. A. (1986). Hook-shaped arcs in dayside polar cap and their relation to the IMF. *Planetary and Space Science*, 34(6), 489–496. [https://doi.org/10.1016/0032-0633\(86\)90087-5](https://doi.org/10.1016/0032-0633(86)90087-5)
- Gussenhoven, M. S. (1982). Extremely high latitude auroras. *Journal of Geophysical Research*, 87(A4), 2401–2412. <https://doi.org/10.1029/JA087iA04p02401>
- Hairston, M. (2018). *Madrigal SSIES-2 manual*. Retrieved from [http://cedar.openmadrigal.org/static/siteSpecific/UT\\_Dallas\\_DMSP\\_Description.pdf](http://cedar.openmadrigal.org/static/siteSpecific/UT_Dallas_DMSP_Description.pdf)
- Hardy, D. A., Burke, W. J., & Gussenhoven, M. S. (1982). DMSP optical and electron measurements in the vicinity of polar cap arcs. *Journal of Geophysical Research*, 87(A4), 2413–2430. <https://doi.org/10.1029/JA087iA04p02413>
- Hardy, D. A., Holeman, E. G., Burke, W. J., Gentile, L. C., & Bounar, K. H. (2008). Probability distributions of electron precipitation at high magnetic latitudes. *Journal of Geophysical Research*, 113, A06305. <https://doi.org/10.1029/2007JA012746>
- Hardy, D. A., Schmitt, L. K., Gussenhoven, M. S., Marshall, F. J., Yeh, H. C., Schumaker, T. L., et al. (1984). *Precipitating electron and ion detectors (SSJ/4) for the Block 5D/Flights 6-10 DMSP satellites: Calibration and data presentation, Technical report AFGL-TR-84-0317*. MA: Hanscom Air Force Base, Air Force Geophysics Laboratory.
- Hardy, D. A., Walton, D. M., Johnstone, A. D., Smith, M. F., Gough, M. P., Huber, A., et al. (1993). Low energy plasma analyzer. *IEEE Transactions on Nuclear Science*, 40(2), 246–251. <https://doi.org/10.1109/23.212349>
- Hosokawa, K., Moen, J. I., Shiokawa, K., & Otsuka, Y. (2011). Motion of polar cap arcs. *Journal of Geophysical Research*, 116, A01305. <https://doi.org/10.1029/2010JA015906>
- Huang, C. Y., Frank, L. A., Peterson, W. K., Williams, D. J., Lennartsson, W., Mitchell, D. G., et al. (1987). Filamentary structures in the magnetotail lobes. *Journal of Geophysical Research*, 92(A3), 2349–2363. <https://doi.org/10.1029/JA092iA03p02349>
- Ismail, S., & Meng, C.-I. (1982). A classification of polar cap auroral arcs. *Planetary and Space Science*, 30(4), 319–330. [https://doi.org/10.1016/0032-0633\(82\)90037-X](https://doi.org/10.1016/0032-0633(82)90037-X)
- Ismail, S., Wallis, D. D., & Cogger, L. L. (1977). Characteristics of polar cap Sun-aligned arcs. *Journal of Geophysical Research*, 82(29), 4741–4749. <https://doi.org/10.1029/JA082i029p04741>
- Kan, J. R., & Burke, W. J. (1985). A theoretical model of polar cap auroral arcs. *Journal of Geophysical Research*, 90(A5), 4171–4177. <https://doi.org/10.1029/JA090iA05p04171>

- King, J., & Papitashvili, N. (2006). *One min and 5-min solar wind data sets at the Earth's bow shock nose*. Retrieved from <https://omniweb.gsfc.nasa.gov/html/HROdocum.html>
- Knight, H. K., Galkin, I. A., Reinisch, B. W., & Zhang, Y. (2018). Auroral ionospheric E region parameters obtained from satellite-based far ultraviolet and ground-based ionosonde observations: Data, methods, and comparisons. *Journal of Geophysical Research: Space Physics*, 123(7), 6065–6089. <https://doi.org/10.1029/2017JA024822>
- Kozlovsky, A., Aikio, A., Turunen, T., Nilsson, H., Sergienko, T., Safargaleev, V., & Kauristie, K. (2007). Dynamics and electric currents of morningside Sun-aligned auroral arcs. *Journal of Geophysical Research*, 112, A06306. <https://doi.org/10.1029/2006JA012244>
- Kullen, A. (2000). The connection between transpolar arcs and magnetotail rotation. *Geophysical Research Letters*, 27(1), 73–76. <https://doi.org/10.1029/1999GL010675>
- Kullen, A. (2012). Transpolar arcs: Summary and recent results. In A. Keiling, E. Donovan, F. Bagenal, & T. Karlsson (Eds.), *Auroral phenomenology and magnetospheric processes: Earth and other planets*, *Geophysical Monograph Series* (pp. 69–80). Washington, DC: American Geophysical Union. <https://doi.org/10.1029/2011GM001183>
- Kullen, A., Brittnacher, M., Cumnock, J. A., & Blomberg, L. G. (2002). Solar wind dependence of the occurrence and motion of polar auroral arcs: A statistical study. *Journal of Geophysical Research*, 107(A11), 1362. <https://doi.org/10.1029/2002JA009245>
- Kullen, A., Cumnock, J. A., & Karlsson, T. (2008). Seasonal dependence and solar wind control of transpolar arc luminosity. *Journal of Geophysical Research*, 113, A08316. <https://doi.org/10.1029/2008JA013086>
- Lühr, H., Warnecke, J. F., & Rother, M. K. A. (1996). An algorithm for estimating field-aligned currents from single spacecraft magnetic field measurements: A diagnostic tool applied to Freja satellite data. *IEEE Transactions on Geoscience and Remote Sensing*, 34(6), 1369–1376. <https://doi.org/10.1109/36.544560>
- Lyons, L. R. (1980). Generation of large-scale regions of auroral currents, electric potentials, and precipitation by the divergence of the convection electric field. *Journal of Geophysical Research*, 85(A1), 17–24. <https://doi.org/10.1029/JA085iA01p00017>
- Milan, S. E., Hubert, B., & Grocott, A. (2005). Formation and motion of a transpolar arc in response to dayside and nightside reconnection. *Journal of Geophysical Research*, 110, A01212. <https://doi.org/10.1029/2004JA010835>
- Neugebauer, M., & Goldstein, R. (1997). Particle and field signatures of coronal mass ejections in the solar wind. In N. Crooker, J. A. Joselyn, & J. Feynman (Eds.), *Coronal mass ejections*, *Geophysical Monograph Series* (pp. 245–251). Washington, DC: American Geophysical Union. <https://doi.org/10.1029/GM099p0245>
- Neugebauer, M., Goldstein, R., & Goldstein, B. E. (1997). Features observed in the trailing regions of interplanetary clouds from coronal mass ejections. *Journal of Geophysical Research*, 102(A9), 19743–19751. <https://doi.org/10.1029/97ja01651>
- Newell, P. T., Burke, W. J., Sánchez, E. R., Meng, C.-I., Greenspan, M. E., & Clauer, C. R. (1991). The low-latitude boundary layer and the boundary plasma sheet at low altitude: Prenoon precipitation regions and convection reversal boundaries. *Journal of Geophysical Research*, 96(A12), 21013–21023. <https://doi.org/10.1029/91JA01818>
- Newell, P. T., Liou, K., & Wilson, G. R. (2009). Polar cap particle precipitation and aurora: Review and commentary. *Journal of Atmospheric and Solar-Terrestrial Physics*, 71(2), 199–215. <https://doi.org/10.1016/j.jastp.2008.11.004>
- Newell, P. T., Wing, S., Meng, C.-I., & Sigillito, V. (1991). The auroral oval position, structure, and intensity of precipitation from 1984 onward: An automated on-line data base. *Journal of Geophysical Research*, 96(A4), 5877–5882. <https://doi.org/10.1029/90JA02450>
- Nowada, M., Fear, R. C., Grocott, A., Shi, Q.-Q., Yang, J., Zong, Q.-G., et al. (2018). Subsidence of ionospheric flows triggered by magnetotail magnetic reconnection during transpolar arc brightening. *Journal of Geophysical Research: Space Physics*, 123(5), 3398–3420. <https://doi.org/10.1029/2017JA024701>
- Nowada, M., Zong, Q.-G., Hubert, B., Shi, Q.-Q., Wang, Y.-F., Yang, J., et al. (2020). North-south asymmetric nightside distorted transpolar arcs within a framework of deformed magnetosphere-ionosphere coupling: IMF-B<sub>y</sub> dependence, ionospheric currents, and magnetotail reconnection, accepted. *Journal of Geophysical Research: Space Physics*, 125, e2020JA027991. <https://doi.org/10.1029/2020JA027991>
- Østgaard, N., Mende, S. B., Frey, H. U., Frank, L. A., & Sigwarth, J. B. (2003). Observations of non-conjugate theta aurora. *Geophysical Research Letters*, 30, 2125. <https://doi.org/10.1029/2003GL017914>
- Østgaard, N., Mende, S. B., Frey, H. U., & Sigwarth, J. B. (2005). Simultaneous imaging of the reconnection spot in the opposite hemispheres during northward IMF. *Geophysical Research Letters*, 32, L21104. <https://doi.org/10.1029/2005GL024491>
- Parker, E. N. (1958). Dynamics of the interplanetary gas and magnetic fields. *The Astrophysical Journal*, 128, 664–676. <https://doi.org/10.1086/146579>
- Park, J.-S., Shue, J.-H., Kim, K.-H., Pi, G., Němeček, Z., & Šafránková, J. (2016). Global expansion of the dayside magnetopause for long-duration radial IMF events: Statistical study on GOES observations. *Journal of Geophysical Research: Space Physics*, 121(7), 6480–6492. <https://doi.org/10.1002/2016JA022772>
- Paxton, L. J., Christensen, A. B., Humm, D. C., Ogorzalek, B. S., Pardoe, C. T., Morrison, D., et al. (1999). Global ultraviolet imager (GUVI): Measuring composition and energy inputs for the NASA Thermosphere Ionosphere Mesosphere Energetics and Dynamics (TIMED) mission. In A. M. Larar (Ed.), *Optical spectroscopic techniques and instrumentation for atmospheric and space research III*, *proc. SPIE* 3756 (pp. 265–276). Bellingham, WA: SPIE. <https://doi.org/10.1117/12.366380>
- Paxton, L. J., Meng, C.-I., Fountain, G. H., Ogorzalek, B. S., Darlington, E. H., Gary, S. A., et al. (1992). Special Sensor Ultraviolet Spectrographic Imager (SSUSI): An instrument description. In S. Chakrabarti, & A. B. Christensen (Eds.), *Instrumentation for planetary and terrestrial atmospheric remote sensing*, *proc. SPIE* 1745 (pp. 2–15). Bellingham, WA: SPIE. <https://doi.org/10.1117/12.60595>
- Petrinec, S. M. (2016). Draping of strongly flow-aligned interplanetary magnetic field about the magnetopause. *Advances in Space Research*, 58(2), 175–180. <https://doi.org/10.1016/j.asr.2015.10.001>
- Pi, G., Němeček, Z., Šafránková, J., Grygorov, K., & Shue, J.-H. (2018). Formation of the dayside magnetopause and its boundary layers under the radial IMF. *Journal of Geophysical Research: Space Physics*, 123(5), 3533–3547. <https://doi.org/10.1029/2018JA025199>
- Pi, G., Shue, J.-H., Chao, J.-K., Němeček, Z., Šafránková, J., & Lin, C.-H. (2014). A reexamination of long-duration radial IMF events. *Journal of Geophysical Research: Space Physics*, 119(9), 7005–7011. <https://doi.org/10.1002/2014JA019993>
- Pi, G., Shue, J.-H., Grygorov, K., Li, H.-M., Němeček, Z., Šafránková, J., et al. (2017). Evolution of the magnetic field structure outside the magnetopause under radial IMF conditions. *Journal of Geophysical Research: Space Physics*, 122(4), 4051–4063. <https://doi.org/10.1002/2015JA021809>
- Reidy, J. A., Fear, R. C., Whiter, D. K., Lanchester, B., Kavanagh, A. J., Milan, S. E., et al. (2018). Interhemispheric survey of polar cap aurora. *Journal of Geophysical Research: Space Physics*, 123(9), 7283–7306. <https://doi.org/10.1029/2017JA025153>
- Reidy, J. A., Fear, R. C., Whiter, D. K., Lanchester, B. S., Kavanagh, A. J., Paxton, L. J., et al. (2017). Multi-instrument observation of simultaneous polar cap auroras on open and closed magnetic field lines. *Journal of Geophysical Research: Space Physics*, 122(4), 4367–4386. <https://doi.org/10.1002/2016JA023718>



- Rezhenov, B. V., & Vardavas, I. M. (1995). A possible mechanism for theta aurora formation. *Annales Geophysicae*, 13(7), 698–703. <https://doi.org/10.1007/s00585-995-0698-3>
- Rich, F. J. (1984). *Fluxgate magnetometer (SSM) for the Defense Meteorological Satellite Program (DMSP) Block 5D-2, Flight 7. Technical report AFGL-TR-84-0225*. MA: Hanscom Air Force Base, Air Force Geophysics Laboratory.
- Rich, F. J. (1994). *Users guide for the topside ionospheric plasma monitor (SSIES, SSIES-2 and SSIES-3) on spacecraft of the Defense Meteorological Satellite Program (DMSP). Volume I: Technical description. Technical report PL-TR-94-2187*. MA: Hanscom Air Force Base, Phillips Laboratory.
- Rodriguez, J. V., Valladares, C. E., Fukui, K., & Gallagher, H. A., Jr. (1997). Antisunward decay of polar cap arcs. *Journal of Geophysical Research*, 102(A12), 27227–27247. <https://doi.org/10.1029/97JA01727>
- Shepherd, S. G. (2014). Altitude-adjusted corrected geomagnetic coordinates: Definition and functional approximations. *Journal of Geophysical Research: Space Physics*, 119(9), 7501–7521. <https://doi.org/10.1002/2014JA020264>
- Shinohara, I., & Kokubun, S. (1996). Statistical properties of particle precipitation in the polar cap during intervals of northward interplanetary magnetic field. *Journal of Geophysical Research*, 101(A1), 69–82. <https://doi.org/10.1029/95JA01848>
- Song, P., DeZeeuw, D. L., Gombosi, T. I., Groth, C. P. T., & Powell, K. G. (1999). A numerical study of solar wind-magnetosphere interaction for northward interplanetary magnetic field. *Journal of Geophysical Research*, 104(A12), 28361–28378. <https://doi.org/10.1029/1999JA900378>
- Song, P., & Vasyliūnas, V. M. (2010). Aspects of global magnetospheric processes. *Chinese Journal of Space Science*, 30(4), 289–311. <https://doi.org/10.11728/cjss2010.04.289>
- Tanaka, T., Obara, T., & Kunitake, M. (2004). Formation of the theta aurora by a transient convection during northward interplanetary magnetic field. *Journal of Geophysical Research*, 109, A09201. <https://doi.org/10.1029/2003JA010271>
- Tang, B. B., Wang, C., & Li, W. Y. (2013). The magnetosphere under the radial interplanetary magnetic field: A numerical study. *Journal of Geophysical Research*, 118(12), 7674–7682. <https://doi.org/10.1002/2013JA019155>
- Valladares, C. E., Carlson, H. C., Jr, & Fukui, K. (1994). Interplanetary magnetic field dependency of stable sun-aligned polar cap arcs. *Journal of Geophysical Research*, 99(A4), 6247–6272. <https://doi.org/10.1029/93ja03255>
- Wang, H., Lühr, H., Shue, J.-H., Frey, H. U., Kervalishvili, G., Huang, T., et al. (2014). Strong ionospheric field-aligned currents for radial interplanetary magnetic fields. *Journal of Geophysical Research: Space Physics*, 119(5), 3979–3995. <https://doi.org/10.1002/2014JA019951>
- Watari, S., Vandas, M., & Watanabe, T. (2005). Solar cycle variation of long-duration radial interplanetary magnetic field events at 1 AU. *Journal of Geophysical Research*, 110, A12102. <https://doi.org/10.1029/2005JA011165>
- Winningham, J. D., & Heikkila, W. J. (1974). Polar cap auroral electron fluxes observed with ISIS 1. *Journal of Geophysical Research*, 79(7), 949–957. <https://doi.org/10.1029/JA079i007p00949>
- Xing, Z., Zhang, Q., Han, D., Zhang, Y., Sato, N., Zhang, S., et al. (2018). Conjugate observations of the evolution of polar cap arcs in both hemispheres. *Journal of Geophysical Research: Space Physics*, 123(3), 1794–1805. <https://doi.org/10.1002/2017JA024272>
- Zhang, Q.-H., Zhang, Y.-L., Wang, C., Lockwood, M., Yang, H.-G., Tang, B.-B., et al. (2020). Multiple transpolar auroral arcs reveal insight about coupling processes in the Earth's magnetotail. *Proceedings of the National Academy of Sciences*, 117(28), 16193–16198. <https://doi.org/10.1073/pnas.2000614117>
- Zhang, Y., Paxton, L. J., Zhang, Q., & Xing, Z. (2016). Polar cap arcs: Sun-aligned or cusp-aligned? *Journal of Atmospheric and Solar-Terrestrial Physics*, 146, 123–128. <https://doi.org/10.1016/j.jastp.2016.06.001>
- Zhu, L., Schunk, R. W., & Sojka, J. J. (1997). Polar cap arcs: A review. *Journal of Atmospheric and Solar-Terrestrial Physics*, 59(10), 1087–1126. [https://doi.org/10.1016/S1364-6826\(96\)00113-7](https://doi.org/10.1016/S1364-6826(96)00113-7)